Science Advances
AAAS

Supplementary Materials for

Simultaneous electromechanical monitoring in engineered heart tissues using a mesoscale framework

Dominic E. Fullenkamp *et al.*

Corresponding author: Yoonseok Park, yoonseok.park@khu.ac.kr; Igor R. Efimov, igor.efimov@northwestern.edu; Elizabeth M. McNally, elizabeth.mcnally@northwestern.edu; John A. Rogers, jrogers@northwestern.edu

The PDF file includes:

Supplementary Text
Figs. S1 to S15
Legends for movies S1 to S4
Legends for data S1 to S5
References

Other Supplementary Material for this manuscript includes the following:

Movies S1 to S4
Data S1 to S5

Supplementary Text

<u>Device stability for long-term evaluation of organoids</u>

Fig. S9 (B) and (C) show the average impedance of each electrode at 1 kHz frequency in 1×PBS solution and the average initial resistance of each strain sensor, respectively. The impedance ranged from 2 to 5 kΩ, and the initial resistance ranged from 1.4 to 1.7 kΩ. We evaluated the durability of the device for long-term evaluation of organoids through accelerated experiments conducted at a temperature of 50°C according to the guidelines of ASTM1980.

$$\text{Accelerated aging time} = \frac{Desired\ real\ time}{Q_{10}^{[(T_{AA}-T_{AMB})/10]}} \qquad (1)$$

where Q_{10} represents aging factor as a constant of 2, T_{AA} denotes the accelerated aging temperature set at 50°C, T_{AMB} represents the in vitro experimental temperature set at 37°C. Fig. S9 D shows a series of optical images from a 37-day accelerated test, corresponding to approximately 90 days in an incubator at 37°C. During this period, the electrode impedance, as expressed in a frequency sweep function from 1 to 10 Hz, showed consistent behavior. Additionally, as depicted in the graph that focuses on measurements at 1 kHz, the impedance remained constant (Fig. S9 E). Tracking the average impedance of each of the six electrodes across five devices at 1 kHz for 37 days reveals no evidence of increasing impedance with time (Fig. S9 F). Similarly, the strain sensors also show no change (Fig. S9 G), indicating that our platform is suitable for long-term evaluation of EHTs and continuous collection of reliable data.

<u>Strain changes associated with transformation from a 2D precursor to a 3D structure</u>

The maximum strain associated with transformation from a 2D precursor to a 3D structure, and then back to the 2D shape again (Fig. S7 A) is approximately 0.13% (Fig. S7 B, *n=10*).

<u>Sampling rate and time latency</u>

Intan amplifiers (INTAN 128 ch RHS Stim/Recording controller with I/O expander, Intan technology) can reconstruct the waveforms of all channels with < 0.2 ms latency. Data acquisition used 16-bit

resolution at a sampling rate of 20 kHz, with a peak duration (R-wave peak time; RWPT) of 10 ± 1.1 ms at 30 randomly selected peaks (Fig. S15 A).

The sampling theorem for signal reconstruction follows the equation:

$$F(t) = \sum_{n=-\infty}^{\infty} Xn \frac{sin\pi(2Wt-n)}{\pi(2Wt-n)}$$

$$Xn = F(\frac{n}{2W}) \qquad (2)$$

$$\therefore Fs > 2\ Fmax$$

$$\text{Peak duration} \times \text{Frequency} = 1 \qquad (3)$$

According to the Shannon-Nyquist theorem, a sampling rate higher than two times Fs guarantees accurate reconstruction. Also, the product of the peak duration and the frequency must be 1. Applying this criterion in this experiment condition yields RWPT = 10 ms, indicating that the peak frequency of the EHT is 100 Hz. According to the Nyquist theorem, the minimum sampling rate required to reconstruct the EHT peak is 200 Hz. The field potential of all EHTs was 20 kHz, which is 100 times higher than the minimum sampling rate of 200 Hz. The maximum latency of the Intan amplifier is 200 μs, across all six channels (Fig. S15 B). The signal obtained from each electrode passes through the amplifier under the same conditions, such that the time latency corresponds to an overall shift in timing and not a relative change, thus enabling a reliable calculation of conduction velocity. The multi-well Axion system (Maestro Pro) has a sampling rate of 12.5 kHz (*23, 53*). The Intan amplifier is also available with high sampling rates up to 30 kHz and 128 channels (*54-56*). Both amplifiers meet requirements for accurate measurement of biological signals through fast data transmission and recording. In addition, our electrophysiological measurements (5.65cm/s) yield a conduction velocity that is similar (~4-15 cm/s) to that in other EHTs found through optical mapping (*18, 57*).

Supplementary Figures
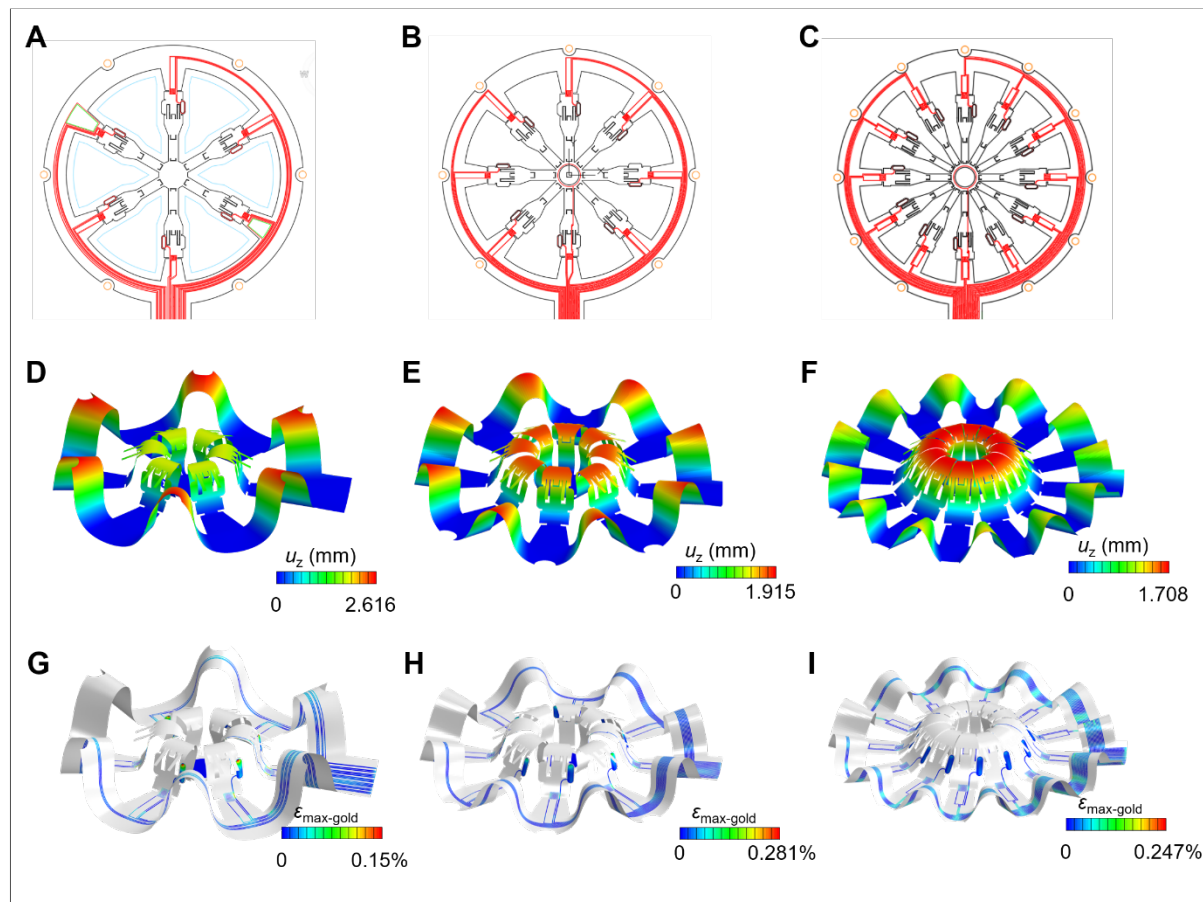
Figure S1. Post number design considerations for 3D-MMF support of EHTs. 2D precursor designs (A-C; red : gold trace, black : device outline) and FEA simulation results (D-I) for corresponding 3D-MMFs. Tilted side views (D,E,F) with out-of-plane displacements in color contours (u_z), and similar representations of the strains in the gold traces (G,H,I) for cases of structures with 6 posts (A,D,G), 8 posts (B,E,H), and 12 posts (C,F,I).
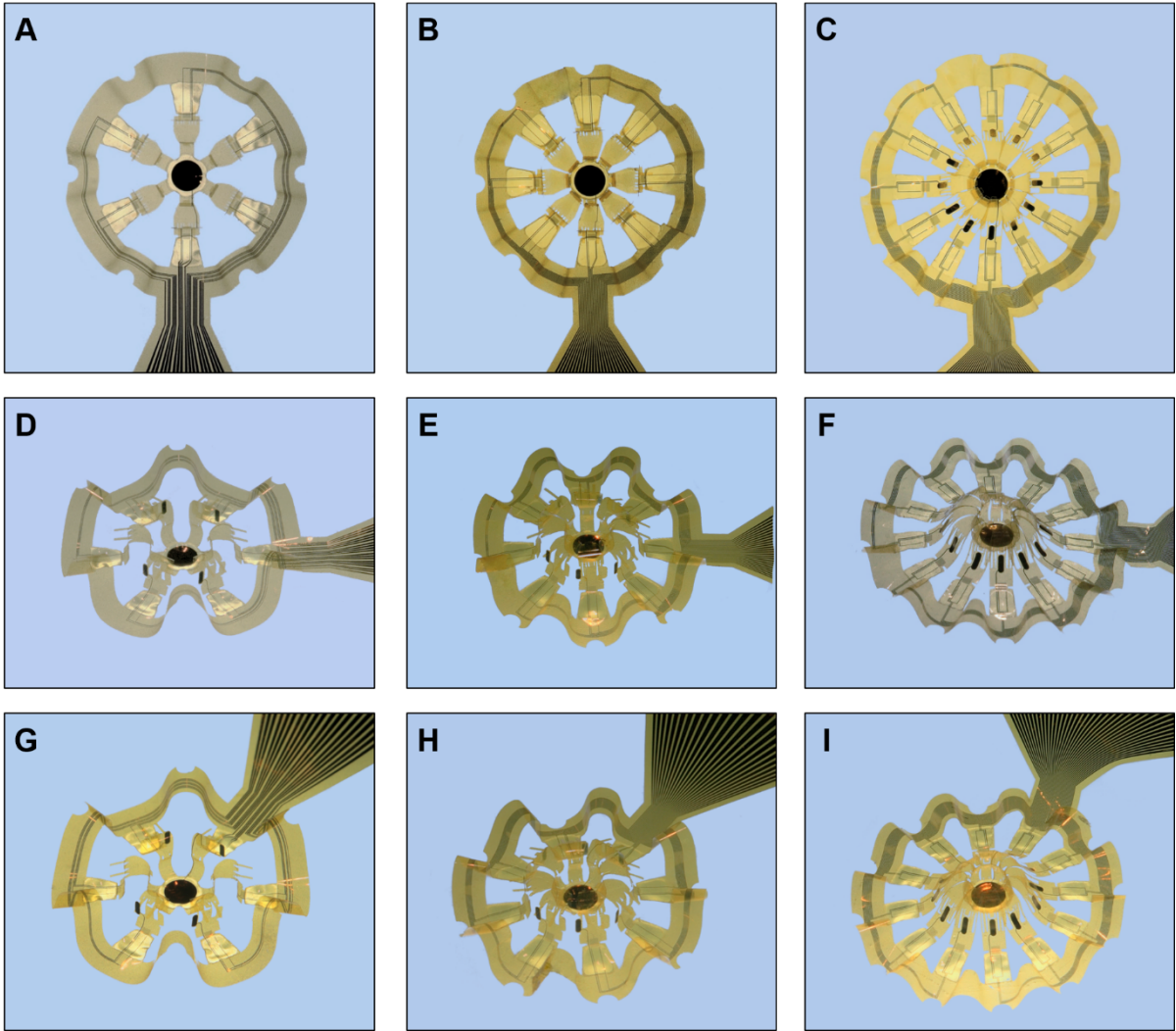
Figure S2. Optical micrographs of alternative post number configurations for 3D-MMFs for support of EHTs. The top-view, side view, and isometric view of structures with 6 posts (A,D,G), 8 posts (B,E,H) and 12 posts (C,F,I).
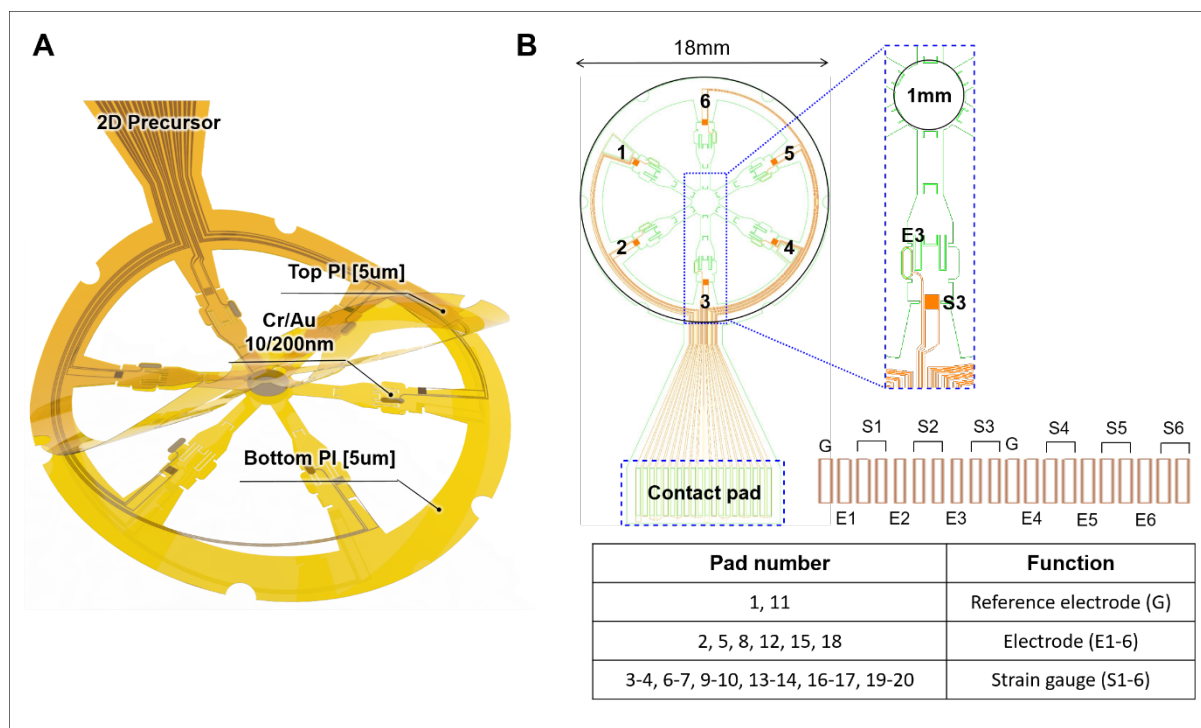
Figure S3. Exploded and planar schematic illustrations of the configuration of the 2D precursor.
(A) Patterns of Cr/Au lie between top and bottom layers of PI with the same thickness (5μm). (B) Layout of the gold pattern, outline of the PI, and pin map information for the electrodes and strain gauges.
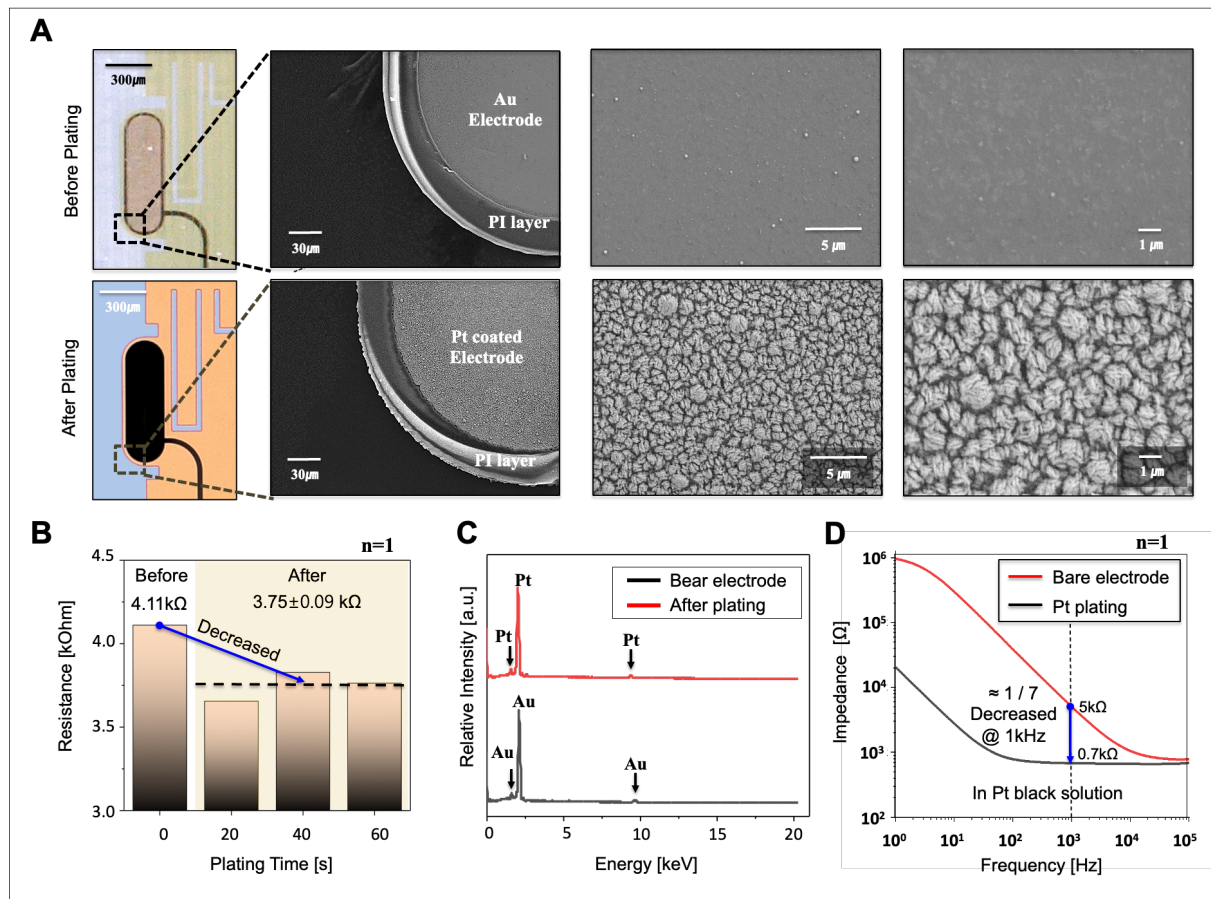
Figure S4. Images and characterization of electroplated Pt black on the sensing/pacing electrodes for low impedance interfaces. (A) Surface morphology defined by optical and FE-SEM imaging for bare Au and Pt-coated electrodes. (B) Example comparison of resistance changes according to electroplating time at #1 electrode. (C) EDS spectrum of before and after Pt electroplating. (D) Impedance data for bare Au electrodes and after Pt electroplating for 60 s, for frequencies from 1 to 10^5 Hz.
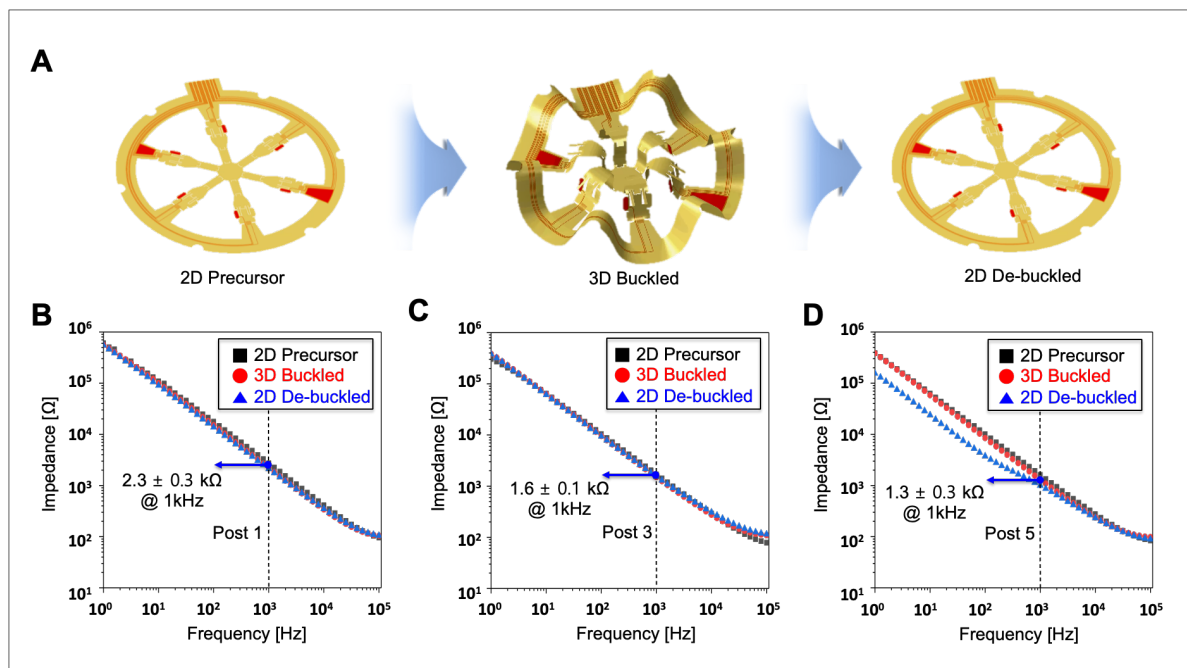
**Figure S5. Characterization of electrode impedance at various stages of forming a 3D-MMF.** 2D precursor, 3D buckling, and 2D de-buckling states were characterized. (A) Schematic illustration of the transformations for corresponding impedance measurement. Impedance as a function of frequency from 1 to 10^5 Hz (B) at post #1, (C) post #3, (D) post #5 (■ 2D precursor, ●3D buckled structure, ▲2D de-buckled structure).
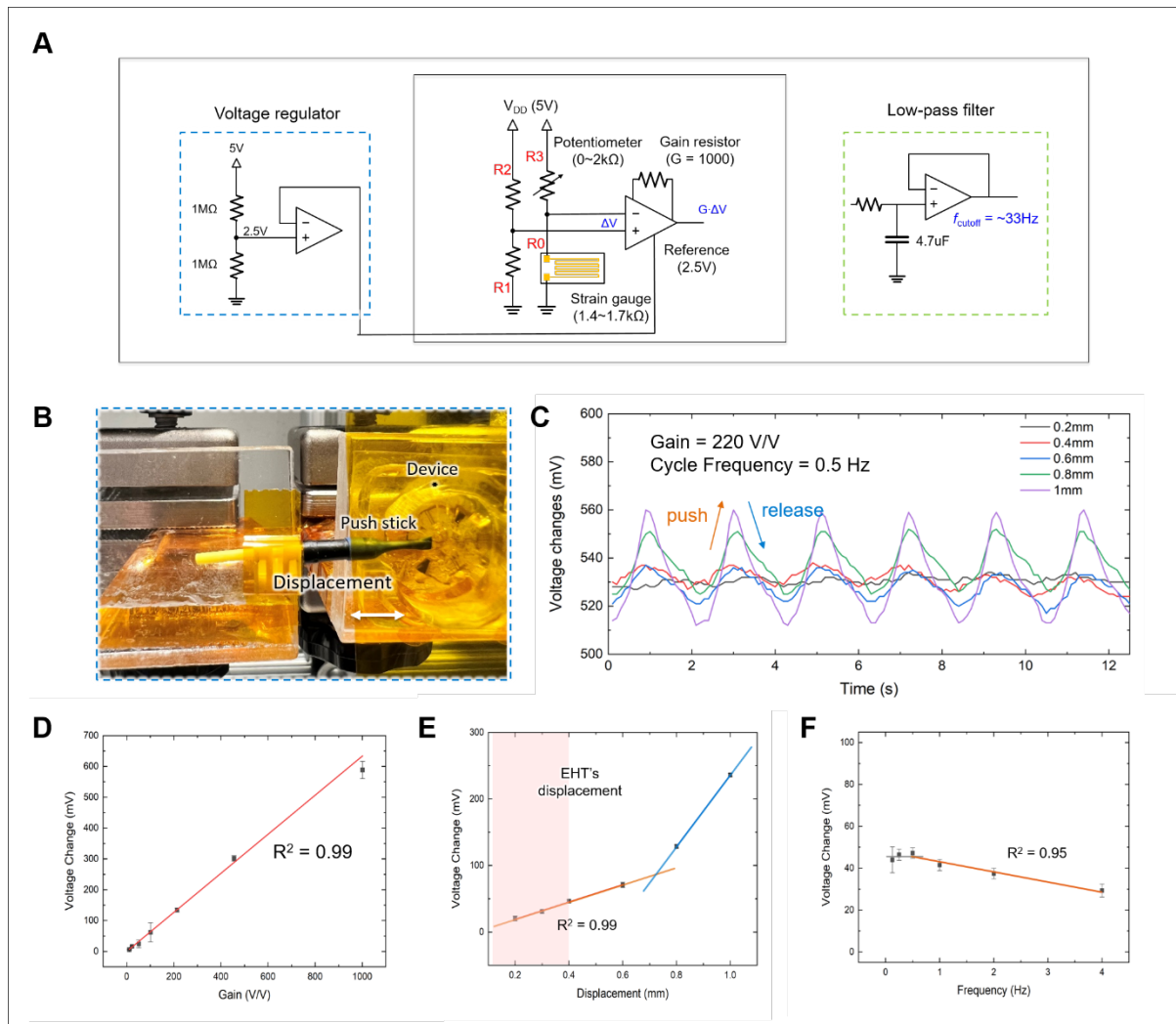
Figure S6. Circuit configuration and characterization of the 3D-MMF strain sensor. (A) Circuit configuration for measuring the responses of the strain sensors using an instrumentation amplifier and low-pass filter. (B) Bench-top setup for measuring the response of a strain sensor to unidirectional external force. (C) Raw data for voltage changes (G×ΔV) obtained from the benchtop test setup with respect to displacements from 0.2 to 1 mm. The gain (G) is 220 V/V, and the cycle frequency is 0.5 Hz. Extracted data for voltage changes obtained from the benchtop test setup as a function of three parameters: (D) Gain, (E) Displacement, and (F) Frequency.
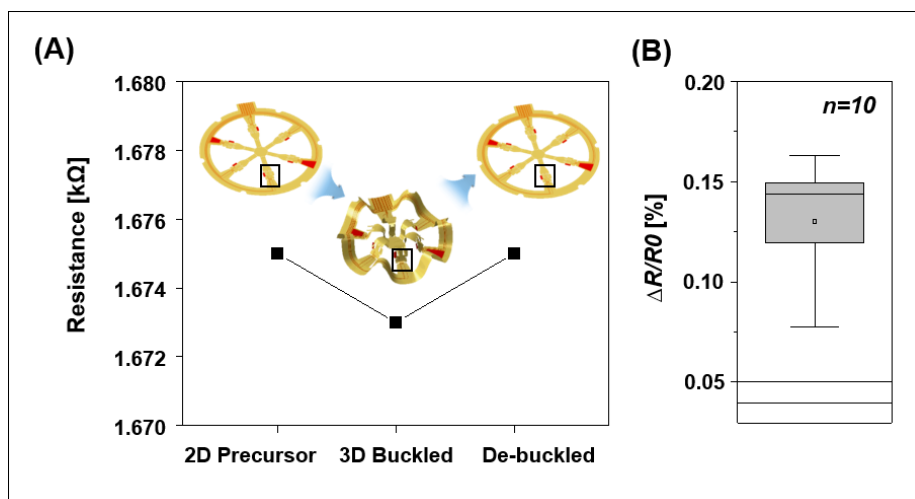
Figure S7. Characterization of the 3D MMF strain sensor in response to de-buckling. (A) Representative changes in resistance associated with transformation of a 2D precursor, into a 3D structure, and then back to the 2D form. (B) Relative changes in resistance *(average; 0.13%, n=10)* of a strain sensor during the transition from a 2D precursor to a 3D structure
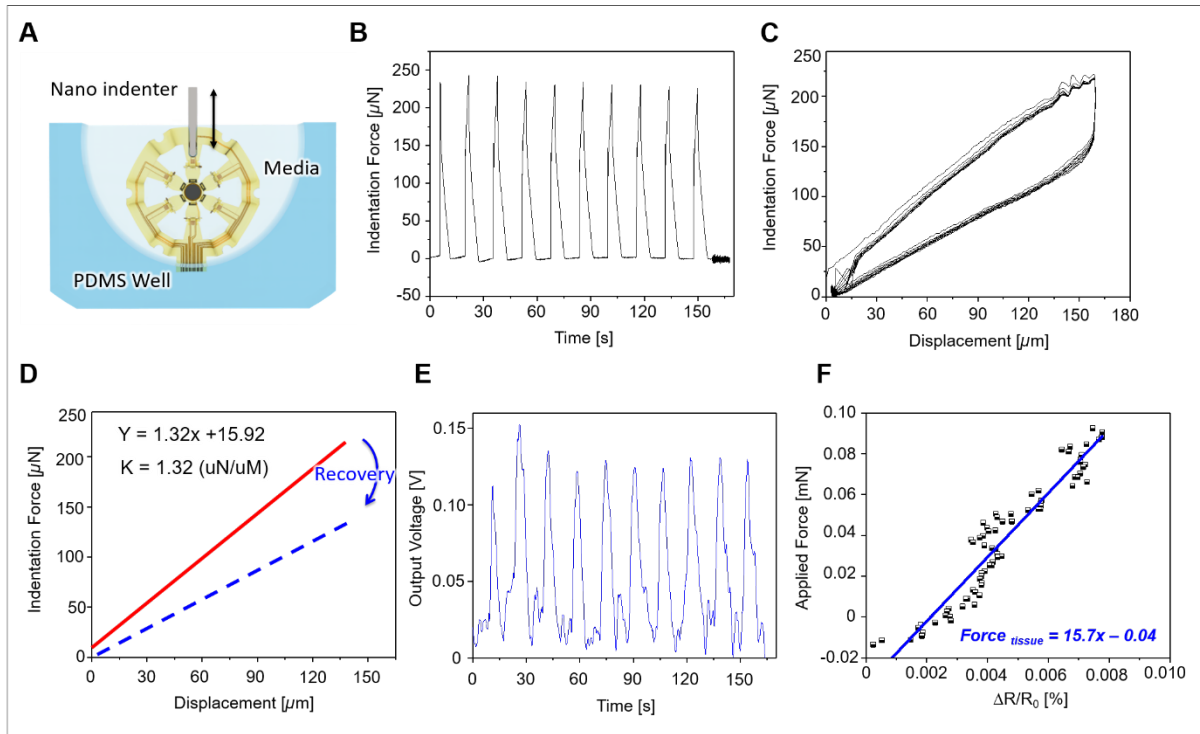
Figure S8. Experimental set-up and characterization of 3D-MMF strain sensors. (A) Schematic diagram of the set-up for measuring applied force and sensor response while immersed in water to mimic operation in vitro. (B) Indentation force measured during 10 repeated cycles of with a crosshead speed of 20 μm/s and displacement from 0 to 160 μm. (C) 10 cycles of overlaid plots of indentation force versus displacement. (D) Bending stiffness obtained as the average slope of the force recorded during application and removal of applied force. (E) Relative change in the output voltage of the strain sensor for linear motion during a cyclic indentation test. (F) Plot of applied force and corresponding relative changes in resistance changes of a strain sensor.
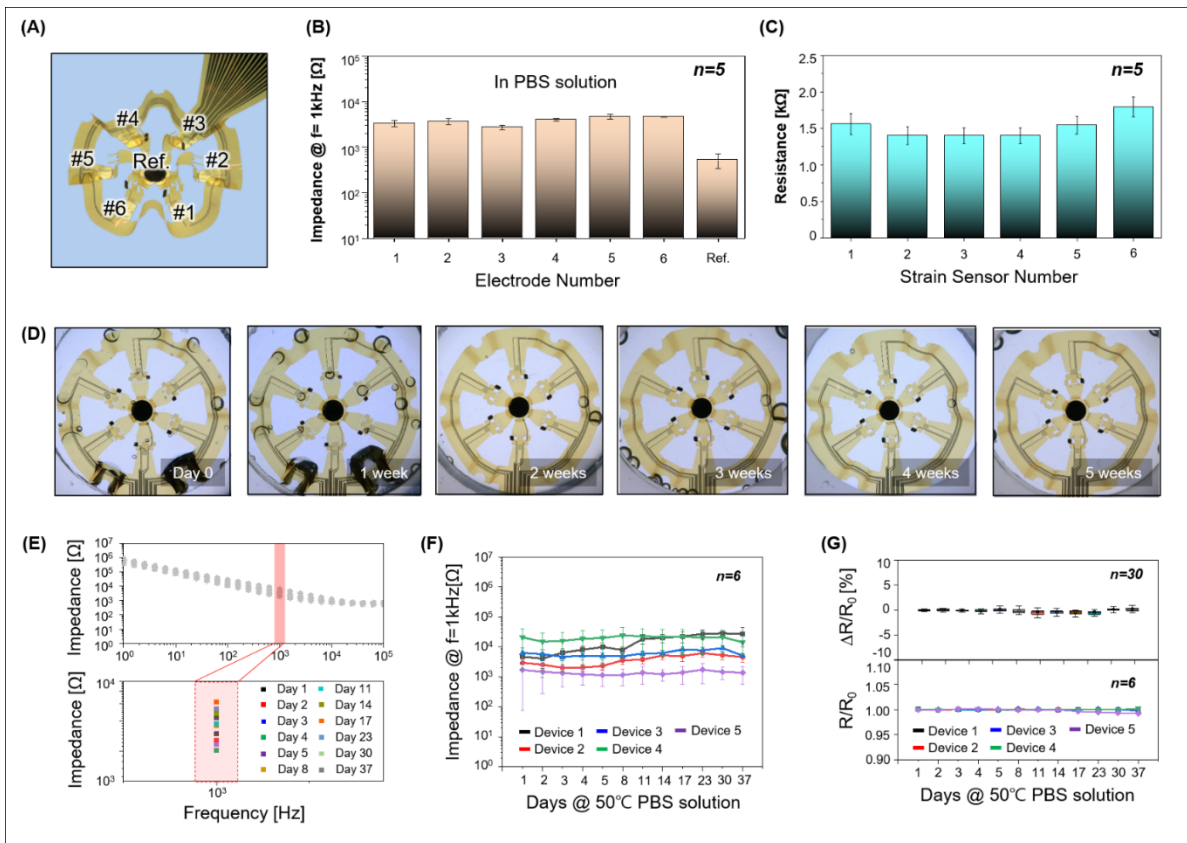
Figure S9. Characterization of performance from device-to-device and day-to-day. (A) Depiction of the positions of posts #1 to 6 and the reference electrode. (B) Average impedance of each electrode at 1kHz in 1x PBS solution *(n=5)*. (C) Average resistance of strain sensors at each location *(n=5)*. (D) A series of optical images showing device stability in 1× PBS (pH 7.4) at a temperature of 50°C. (E) Representative impedance as a function of frequency from 1 to 10^5 Hz over a period of up to 5 weeks (upper). Magnified view of impedance values at 1 kHz measured on various dates (lower). (F) Average impedance changes at 1 kHz for 6 electrodes in each device immersed in 50°C 1x PBS solution for up to 5 weeks. (G) Average resistance changes for 6 strain sensors in each device immersed in 50°C 1x PBS solution over a period of up to 5 weeks.
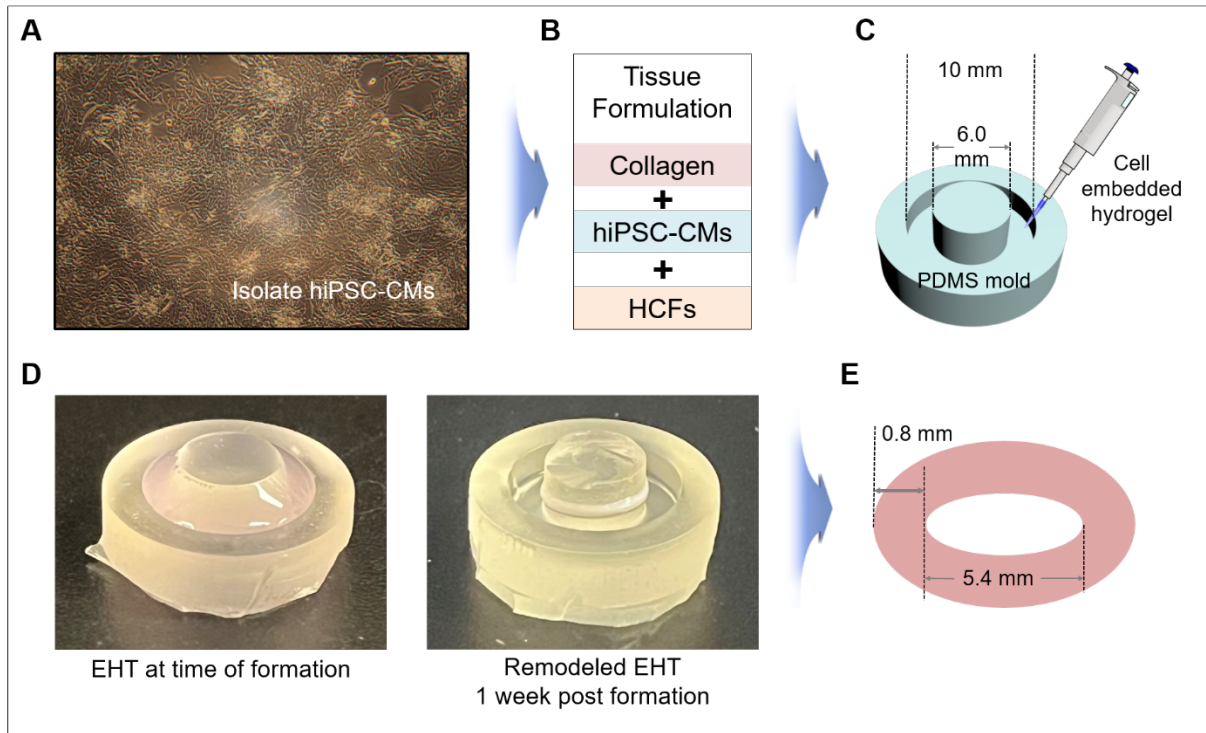
Figure S10. Process of EHT creation and remodeling. (A) Optical image of isolated hiPSC-CMs. (B) Tissue formation of cells embedded in a collagen-based hydrogel for casting into a circular mold. (C) Geometry and size parameters for a customized PDMS mold. (D) Optical images of EHTs formation after casting into a mold, and remodeled EHTs after 1 week post formation. (E) Dimensions of free-floating EHTs separated from the mold before transfer to a 3D-MMF.
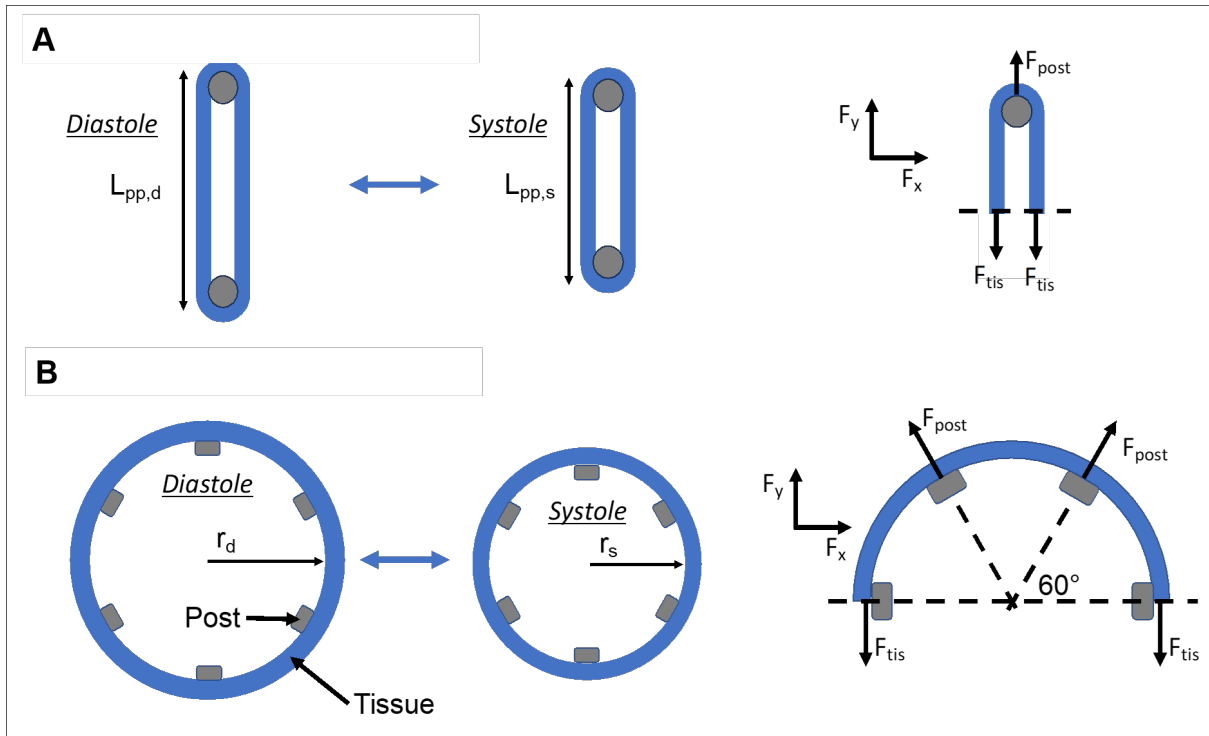
Figure S11. **Schematic diagram of EHT loading conditions.** (A) Traditional 2 post model (● post, ■ tissue; $L_{pp,d}$: diameter of diastolic (resting) length of the tissue, $L_{pp,s}$: diameter of systolic length of the tissue, F_{post} : force of post, F_{tis} : force of tissue). (B) Circular 6 post model for integrating on a 3D MMF (r_d : radius of diastole, r_s : radius of systole).
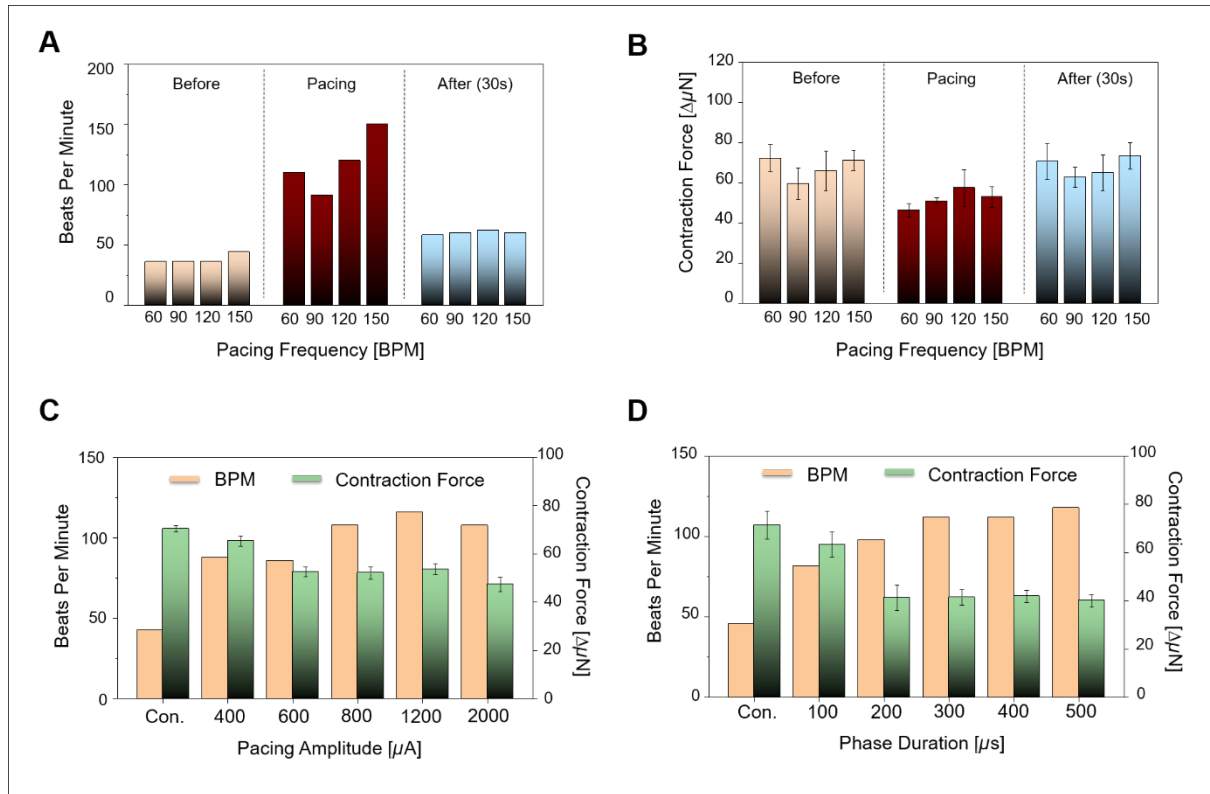
Figure S12. Example of pacing response in beats per minute (bpm) and contractile force measurements. (A) Changes in bpm and **(B)** contractile force according to pacing frequency from 60 to 150 bpm with amplitude of 700 µA, phase duration of 300 µs. **(C)** Changes in bpm and contractile force versus pacing amplitude with frequency of 90 bpm and phase duration of 300 µs. **(D)** bpm and contractile force changes according to phase duration with frequency of 90 bpm and amplitude of 700 µA.
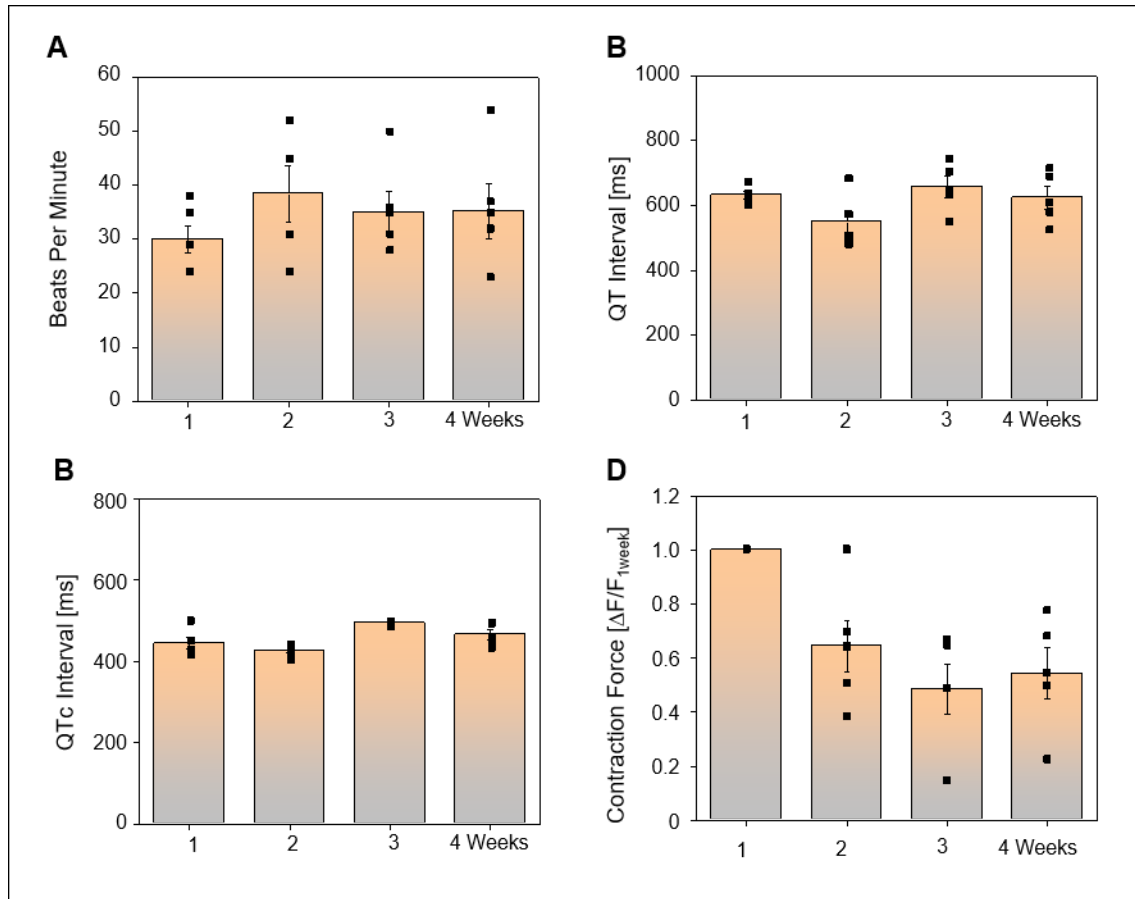
Figure S13. Characterization of EHT performance over time. Observation of normal EHTs activity for 1 week after mounting to 4 weeks *(n=5)*. (A) beat per minute (bpm), (B) Averaged QT interval for 10 cycles, (C) Averaged QTc time for 10 cycles, (D) Averaged contractile tissue force for 10 cycles.
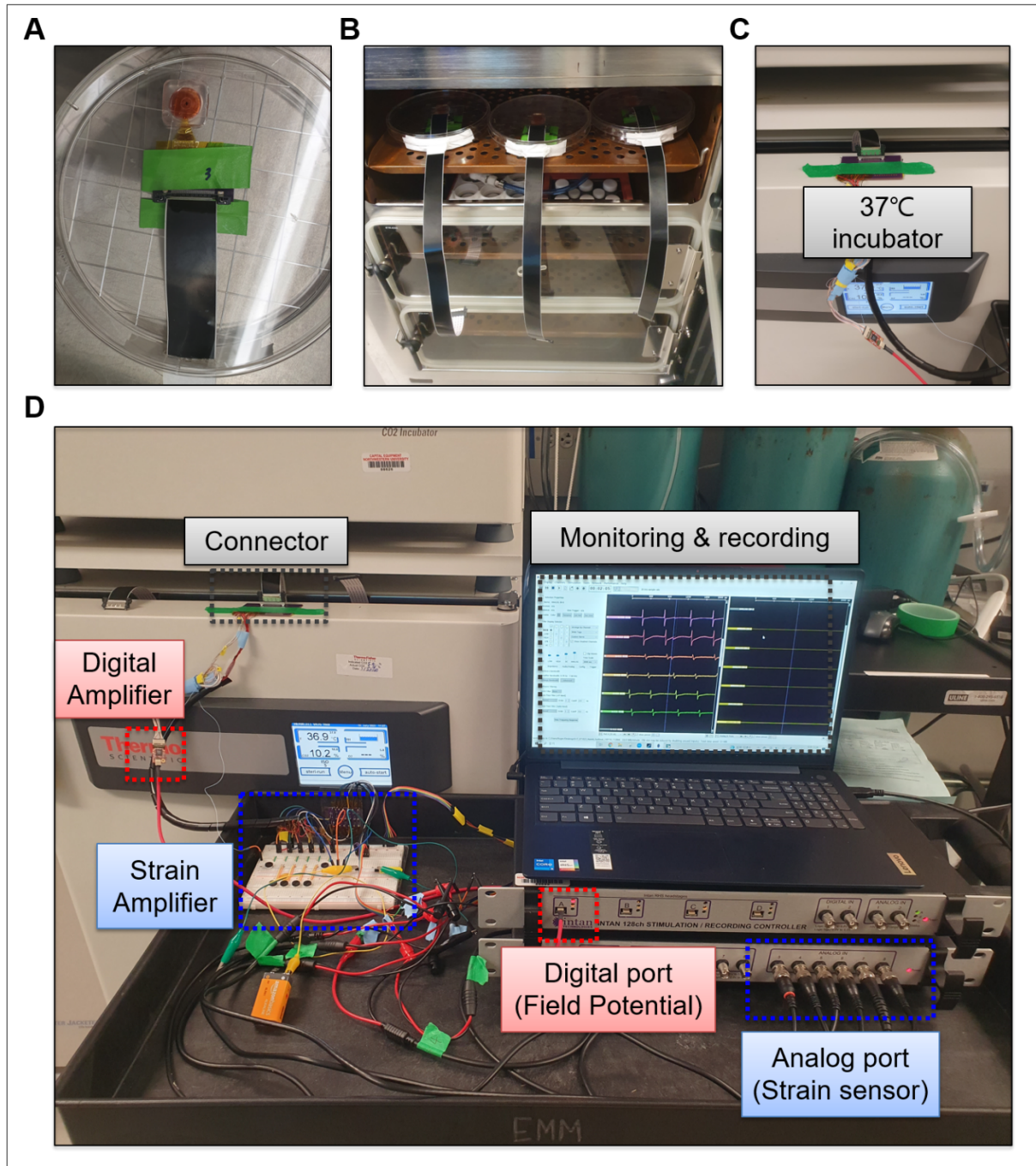
Figure S14. Time synchronized *in vitro* experimental set-up. (A) Image of a device in a petri dish to maintain the sterility of the EHT mounted into the device. (B) Image of each sample, prepared for measurement using an extension cable from the incubator. (C) Connection between the device located in the 37°C incubator and the external measurement electronics. (D) Overall setup to acquire signal from EHTs.
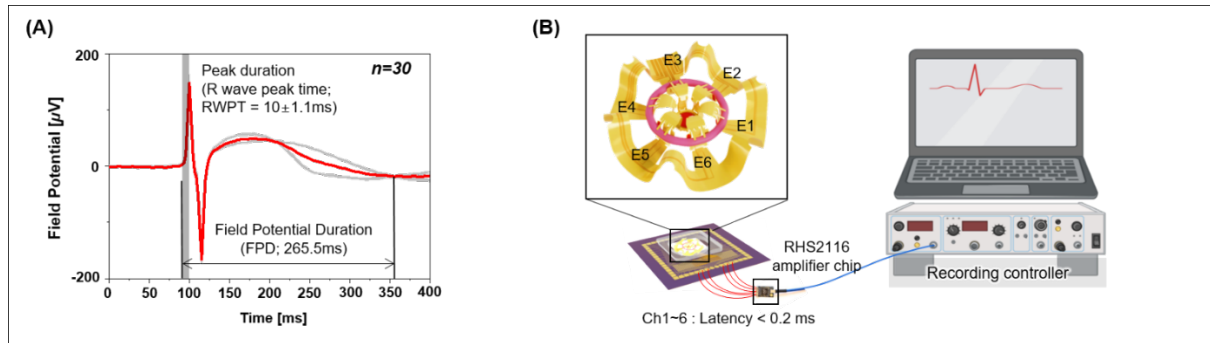
Figure S15. Considerations for sampling rate and time latency. (A) Representative field potential plots for 30 randomly selected peaks recorded from EHTs. The R-wave peak time (RWPT; 10±1 ms) is the signal duration used to determine the minimum sampling rate. The duration of 1 cycle of field potential (FPD; 265.5ms, *n=30*) allows for a calculation of the effect of amplifier signal latency. (B) Schematic diagram of signal acquisition from the EHT, through the RHS2116 amplifier, and into the recording controller. This setup consistently accommodates this latency across all six channels.

Movie S1. Simultaneous monitoring of optical movement, field potential, and strain sensors using the 3D-MMF EHT platform. The first video shows each post capturing the field potential and local force of contraction with optical measurements correlating with the strain sensor measurements shown over 5 spontenous EHT beats. The second video shows at 0.025x speed a single spontaneous beat with the captured field potential.

Movie S2. Tracking EHT deformation field. Optical measurements and tracking of the EHT deformation field on the 3D-MMF over 10 spontaneous EHT beats.

Movie S3. EHT pacing using the 3D-MMF. One of the six MMF electrodes was used to pace the EHT non-invasively. The EHT is shown to beat spontaneously, then paced, and then again beat spontaneously.

Movie S4. Normal and rentrant EHT beating. An EHT is seen to beat spontaneously on the 3D-MMF and after it is induced into reentry.

Data S1. Figure 1 source data. This file contains Figure 1 source data.

Data S2. Figure 2 source data. This file contains Figure 2 source data. Note Figure 2L source data is included in **Data S5**.

Data S3. Figure 3 source data. This file contains Figure 3 source data.

Data S4. Figure 4 source data. This file contains Figure 4 source data.

Data S5. Figure 2L source data. This file contains Figure 2L source data.

REFERENCES AND NOTES

1. B. Yu, S. R. Zhao, C. D. Yan, M. Zhang, J. C. Wu, Deconvoluting the cells of the human heart with iPSC technology: Cell types, protocols, and uses. *Curr. Cardiol. Rep.* **24**, 487–496 (2022).

2. P. W. Burridge, A. Holmström, J. C. Wu, Chemically defined culture and cardiomyocyte differentiation of human pluripotent stem cells. *Curr. Protoc. Hum. Genet.* **87**, 21.3.1–21.3.15 (2015).

3. S. R. Houser, K. B. Margulies, A. M. Murphy, F. G. Spinale, G. S. Francis, S. D. Prabhu, H. A. Rockman, D. A. Kass, J. D. Molkentin, M. A. Sussman, W. J. Koch; American Heart Association Council on Basic Cardiovascular Sciences, Council on Clinical Cardiology, and Council on Functional Genomics and Translational Biology,Animal models of heart failure: A scientific statement from the American Heart Association. *Circ. Res.* **111**, 131–150 (2012).

4. K. Nakao, W. Minobe, R. Roden, M. R. Bristow, L. A. Leinwand, Myosin heavy chain gene expression in human heart failure. *J. Clin. Invest.* **100**, 2362–2370 (1997).

5. S. Schiaffino, A. C. Rossi, V. Smerdu, L. A. Leinwand, C. Reggiani, Developmental myosins: Expression patterns and functional significance. *Skelet. Muscle* **5**, 22 (2015).

6. J. Montag, B. Petersen, A. Flögel, E. Becker, A. Lucas-Hahn, G. Cost, C. Mühlfeld, T. Kraft, H. Niemann, B. Brenner, Successful knock-in of hypertrophic cardiomyopathy-mutation R723G into the MYH7 gene mimics HCM pathology in pigs. *Sci. Rep.* **8**, 4786 (2018).

7. M. Wadman, FDA no longer has to require animal testing for new drugs. *Science* **379**, 127–128 (2023).

8. J. J. Han, FDA Modernization Act 2.0 allows for alternatives to animal testing. *Artif. Organs* **47**, 449–450 (2023).

9. N. Sayed, C. Liu, J. C. Wu, Translation of human-induced pluripotent stem cells: From clinical trial in a dish to precision medicine. *J. Am. Coll. Cardiol.* **67**, 2161–2176 (2016).

10. C. Tu, B. S. Chao, J. C. Wu, Strategies for improving the maturity of human induced pluripotent stem cell-derived cardiomyocytes. *Circ Res*. **123**, 512–514 (2018); https://doi.org/10.1161/CIRCRESAHA.118.313472.

11. I. Karakikes, M. Ameen, V. Termglinchan, J. C. Wu, Human induced pluripotent stem cell–derived cardiomyocytes: Insights into molecular, cellular, and functional phenotypes. *Circ. Res.* **117**, 80–88 (2015).

12. M. Tiburcy, J. E. Hudson, P. Balfanz, S. Schlick, T. Meyer, Mei-Ling Chang Liao, E. Levent, F. Raad, S. Zeidler, E. Wingender, J. Riegler, M. Wang, J. D. Gold, I. Kehat, E. Wettwer, U. Ravens, P. Dierickx, Linda W van Laake, M. J. Goumans, S. Khadjeh, K. Toischer, G. Hasenfuss, L. A. Couture, A. Unger, W. A. Linke, T. Araki, B. Neel, G. Keller, L. Gepstein, J. C. Wu, W.-H. Zimmermann, Defined engineered human myocardium with advanced maturation for applications in heart failure modeling and repair. *Circulation* **135**, 1832–1847 (2017).

13. K. Breckwoldt, D. Letuffe-Brenière, I. Mannhardt, T. Schulze, B. Ulmer, T. Werner, A. Benzin, B. Klampe, M. C. Reinsch, S. Laufer, A. Shibamiya, M. Prondzynski, G. Mearini, D. Schade, S. Fuchs, C. Neuber, E. Krämer, U. Saleem, M. L. Schulze, M. L. Rodriguez, T. Eschenhagen, A. Hansen, Differentiation of cardiomyocytes and generation of human engineered heart tissue. *Nat. Protoc.* **12**, 1177–1197 (2017).

14. J. Schwan, A. T. Kwaczala, T. J. Ryan, O. Bartulos, Y. Ren, L. R. Sewanan, A. H. Morris, D. L. Jacoby, Y. Qyang, S. G. Campbell, Anisotropic engineered heart tissue made from laser-cut decellularized myocardium. *Sci. Rep.* **6**, 32068 (2016).

15. I. Mannhardt, K. Breckwoldt, D. Letuffe-Brenière, S. Schaaf, H. Schulz, C. Neuber, A. Benzin, T. Werner, A. Eder, T. Schulze, B. Klampe, T. Christ, M. N. Hirt, N. Huebner, A. Moretti, T. Eschenhagen, A. Hansen, Human engineered heart tissue: Analysis of contractile force. *Stem Cell Reports* **7**, 29–42 (2016).

16. J. M. Bliley, M. Vermeer, R. M. Duffy, I. Batalov, D. Kramer, J. W. Tashman, D. J. Shiwarski, A. Lee, A. S. Teplenin, L. Volkers, B. Coffin, M. F. Hoes, A. Kalmykov, R. N. Palchesko, Y. Sun, J. D. H. Jongbloed, N. Bomer, R. A. de Boer, A. J. H. Suurmeijer, D. A. Pijnappels, M. C. Bolling, P. van der Meer, A. W. Feinberg, Dynamic loading of human engineered heart tissue enhances contractile function and drives a desmosome-linked disease phenotype. *Sci. Transl. Med.* **13**, eabd1817 (2021).

17. M. Kim, J. C. Hwang, S. Min, Y.-G. Park, S. Kim, E. Kim, H. Seo, W. G. Chung, J. Lee, S.-W. Cho, J.-U. Park, Multimodal characterization of cardiac organoids using integrations of pressure-sensitive transistor arrays with three-dimensional liquid metal electrodes. *Nano Lett.* **22**, 7892–7901 (2022).

18. I. Goldfracht, S. Protze, A. Shiti, N. Setter, A. Gruber, N. Shaheen, Y. Nartiss, G. Keller, L. Gepstein, Generating ring-shaped engineered heart tissues from ventricular and atrial human pluripotent stem cell-derived cardiomyocytes. *Nat. Commun.* **11**, 75 (2020).

19. N. V. Chavali, D. O. Kryshtal, S. S. Parikh, L. Wang, A. M. Glazer, D. J. Blackwell, B. M. Kroncke, M. B. Shoemaker, B. C. Knollmann, Patient-independent human induced pluripotent stem cell model: A new tool for rapid determination of genetic variant pathogenicity in long QT syndrome. *Heart Rhythm* **16**, 1686–1695 (2019).

20. W. Dou, A. Daoud, X. Chen, T. Wang, M. Malhi, Z. Gong, F. Mirshafiei, M. Zhu, G. Shan, X. Huang, Ultrathin and flexible bioelectronic arrays for functional measurement of iPSC-cardiomyocytes under cardiotropic drug administration and controlled microenvironments. *Nano Lett.* **23**, 2321–2331 (2023).

21. H. Chen, B. Jiang, J. G. Shamul, X. He, Image entropy-based label-free functional characterization of human induced pluripotent stem cell-derived 3D cardiac spheroids. *Biosens. Bioelectron.* **179**, 113055 (2021).

22. Z. Xie, R. Avila, Y. Huang, J. A. Rogers, Flexible and stretchable antennas for biointegrated electronics. *Adv. Mater.* **32**, e1902767 (2020).

23. Y. Park, C. K. Franz, H. Ryu, H. Luan, K. Y. Cotton, J. U. Kim, T. S. Chung, S. Zhao, A. Vazquez-Guardado, D. S. Yang, K. Li, R. Avila, J. K. Phillips, M. J. Quezada, H. Jang, S. S. Kwak, S. M. Won, K. Kwon, H. Jeong, A. J. Bandodkar, M. Han, H. Zhao, G. R. Osher, H. Wang, K. H. Lee, Y. Zhang, Y. Huang, J. D. Finan, J. A. Rogers, Three-dimensional, multifunctional neural interfaces for cortical spheroids and engineered assembloids. *Sci. Adv.* **7**, eabf9153 (2021).

24. Q. Huang, B. Tang, J. C. Romero, Y. Yang, S. K. Elsayed, G. Pahapale, T.-J. Lee, I. E. M. Pantoja, F. Han, C. Berlinicke, T. Xiang, M. Solazzo, T. Hartung, Z. Qin, B. S. Caffo, L. Smirnova, D. H. Gracias, Shell microelectrode arrays (MEAs) for brain organoids. *Sci. Adv.* **8**, eabq5031 (2022).

25. A. Kalmykov, C. Huang, J. Bliley, D. Shiwarski, J. Tashman, A. Abdullah, S. K. Rastogi, S. Shukla, E. Mataev, A. W. Feinberg, K. J. Hsia, T. Cohen-Karni, Organ-on-e-chip: Three-dimensional self-rolled biosensor array for electrical interrogations of human electrogenic spheroids. *Sci. Adv.* **5**, eaax0729 (2019).

26. Y. S. Choi, H. Jeong, R. T. Yin, R. Avila, A. Pfenniger, J. Yoo, J. Y. Lee, A. Tzavelis, Y. J. Lee, S. W. Chen, H. S. Knight, S. Kim, H.-Y. Ahn, G. Wickerson, A. Vázquez-Guardado, E. Higbee-Dempsey, B. A. Russo, M. A. Napolitano, T. J. Holleran, L. A. Razzak, A. N. Miniovich, G. Lee, B. Geist, B. Kim, S. Han, J. A. Brennan, K. Aras, S. S. Kwak, J. Kim, E. A. Waters, X. Yang, A. Burrell, K. S. Chun, C. Liu, C. Wu, A. Y. Rwei, A. N. Spann, A. Banks, D. Johnson, Z. J. Zhang, C. R. Haney, S. H. Jin, A. V. Sahakian, Y. Huang, G. D. Trachiotis, B. P. Knight, R. K. Arora, I. R. Efimov, J. A. Rogers, A transient, closed-loop network of wireless, body-integrated devices for autonomous electrotherapy. *Science* **376**, 1006–1012 (2022).

27. S. Xu, Z. Yan, K.-I. Jang, W. Huang, H. Fu, J. Kim, Z. Wei, M. Flavin, J. M. Cracken, R. Wang, A. Badea, Y. Liu, D. Xiao, G. Zhou, J. Lee, H. U. Chung, H. Cheng, W. Ren, A. Banks, X. Li, U. Paik, R. G. Nuzzo, Y. Huang, Y. Zhang, J. A. Rogers, Assembly of micro/nanomaterials into complex, three-dimensional architectures by compressive buckling. *Science* **347**, 154–159 (2015).

28. H. Ryu, Y. Park, H. Luan, G. Dalgin, K. Jeffris, H.-J. Yoon, T. S. Chung, J. U. Kim, S. S. Kwak, G. Lee, H. Jeong, J. Kim, W. Bai, J. Kim, Y. H. Jung, A. K. Tryba, J. W. Song, Y. Huang, L. H. Philipson, J. D. Finan, J. A. Rogers, Transparent, compliant 3D mesostructures for precise evaluation of mechanical characteristics of organoids. *Adv. Mater.* **33**, e2100026 (2021).

29. M. H. Drazner, The progression of hypertensive heart disease. *Circulation* **123**, 327–334 (2011).

30. M. Tiburcy, T. Meyer, N. Y. Liaw, W.-H. Zimmermann, Generation of engineered human myocardium in a multi-well format. *STAR Protoc.* **1**, 100032 (2020).

31. J. W. Buikema, S. Lee, W. R. Goodyer, R. G. Maas, O. Chirikian, G. Li, Y. Miao, S. L. Paige, D. Lee, H. Wu, D. T. Paik, S. Rhee, L. Tian, F. X. Galdos, N. Puluca, B. Beyersdorf, J. Hu, A. Beck, S. Venkamatran, S. Swami, P. Wijnker, M. Schuldt, L. M. Dorsch, A. van Mil, K. Red-Horse, J. Y. Wu, C. Geisen, M. Hesse, V. Serpooshan, S. Jovinge, B. K. Fleischmann, P. A. Doevendans, J. van der Velden, K. C. Garcia, J. C. Wu, J. P. G. Sluijter, S. M. Wu, Wnt activation and reduced cell-cell contact synergistically induce massive expansion of functional human iPSC-derived cardiomyocytes. *Cell Stem Cell* **27**, 50–63 e5 (2020).

32. A. Rhoden, T. Schulze, N. Pietsch, T. Christ, A. Hansen, T. Eschenhagen, Comprehensive analyses of the inotropic compound omecamtiv mecarbil in rat and human cardiac preparations. *Am. J. Physiol. Heart Circ. Physiol.* **322**, H373–H385 (2022).

33. S. H. Thomas, E. R. Behr, Pharmacological treatment of acquired QT prolongation and torsades de pointes. *Br. J. Clin. Pharmacol.* **81**, 420–427 (2016).

34. H. T. Dodge, J. D. Lord, H. Sandler, Cardiovascular effects of isoproterenol in normal subjects and subjects with congestive heart failure. *Am. Heart J.* **60**, 94–105 (1960).

35. E. G. Navarrete, P. Liang, F. Lan, V. Sanchez-Freire, C. Simmons, T. Gong, A. Sharma, P. W. Burridge, B. Patlolla, A. S. Lee, H. Wu, R. E. Beygui, S. M. Wu, R. C. Robbins, D. M. Bers, J. C. Wu, Screening drug-induced arrhythmia [corrected] using human induced pluripotent stem cell-derived cardiomyocytes and low-impedance microelectrode arrays. *Circulation* **128**, S3–S13 (2013).

36. C. Funck-Brentano, Y. Kibleur, F. Le Coz, J. M. Poirier, A. Mallet, P. Jaillon, Rate dependence of sotalol-induced prolongation of ventricular repolarization during exercise in humans. *Circulation* **83**, 536–545 (1991).

37. J. R. Teerlink, R. Diaz, G. M. Felker, J. J. V. Mc Murray, M. Metra, S. D. Solomon, K. F. Adams, I. Anand, A. Arias-Mendoza, T. Biering-Sørensen, M. Böhm, D. Bonderman, J. G. F. Cleland, R. Corbalan, M. G. Crespo-Leiro, U. Dahlström, L. E. Echeverria, J. C. Fang, G. Filippatos, C. Fonseca, E. Goncalvesova, A. R. Goudev, J. G. Howlett, D. E. Lanfear, J. Li, M. Lund, P. Macdonald, V. Mareev, S.-I. Momomura, E. O'Meara, A. Parkhomenko, P. Ponikowski, F. J. A. Ramires, P. Serpytis, K. Sliwa, J. Spinar, T. M. Suter, J. Tomcsanyi, H. Vandekerckhove, D. Vinereanu, A. A. Voors, M. B. Yilmaz, F. Zannad, L. Sharpsten, J. C. Legg, C. Varin, N. Honarpour, S. A. Abbasi, F. I. Malik, C. E. Kurtz, GALACTIC-HF Investigators,Cardiac myosin activation with omecamtiv mecarbil in systolic heart failure. *N. Engl. J. Med.* **384**, 105–116 (2021).

38. F. I. Malik, J. J. Hartman, K. A. Elias, B. P. Morgan, H. Rodriguez, K. Brejc, R. L. Anderson, S. H. Sueoka, K. H. Lee, J. T. Finer, R. Sakowicz, R. Baliga, D. R. Cox, M. Garard, G. Godinez, R. Kawas, E. Kraynack, D. Lenzi, P. P. Lu, A. Muci, C. Niu, X. Qian, D. W. Pierce, M. Pokrovskii, I. Suehiro, S. Sylvester, T. Tochimoto, C. Valdez, W. Wang, T. Katori, D. A. Kass, Y.-T. Shen, S. F. Vatner, D. J. Morgans, Cardiac myosin activation: A potential therapeutic approach for systolic heart failure. *Science* **331**, 1439–1443 (2011).

39. V. J. Planelles-Herrero, J. J. Hartman, J. Robert-Paganin, F. I. Malik, A. Houdusse, Mechanistic and structural basis for activation of cardiac myosin force production by omecamtiv mecarbil. *Nat. Commun.* **8**, 190 (2017).

40. Y. T. Shen, F. I. Malik, X. Zhao, C. Depre, S. K. Dhar, P. Abarzua, D. J. Morgans, S. F. Vatner, Improvement of cardiac function by a cardiac Myosin activator in conscious dogs with systolic heart failure. *Circ. Heart Fail.* **3**, 522–527 (2010).

41. F. Morady, A. Kadish, M. de Buitleir, W. H. Kou, H. Calkins, S. Schmaltz, S. Rosenheck, J. Sousa, Prospective comparison of a conventional and an accelerated protocol for programmed ventricular stimulation in patients with coronary artery disease. *Circulation* **83**, 764–773 (1991).

42. H. Zhao, Y. Kim, H. Wang, X. Ning, C. Xu, J. Suh, M. Han, G. J. Pagan-Diaz, W. Lu, H. Li, W. Bai, O. Aydin, Y. Park, J. Wang, Y. Yao, Y. He, M. T. A. Saif, Y. Huang, R. Bashir, J. A. Rogers, Compliant 3D frameworks instrumented with strain sensors for characterization of millimeter-scale engineered muscle tissues. *Proc. Natl. Acad. Sci. U.S.A.* **118**, e2100077118 (2021).

43. G. R. Mines, On dynamic equilibrium in the heart. *J. Physiol.* **46**, 349–383 (1913).

44. W. E. Garrey, The nature of fibrillary contraction of the heart.—Its relation to tissue mass and form. *Am. J. Physiol.* **33**, 397–414 (1914).

45. T. Lewis, *The mechanism and graphic registration of the heart beat* (Shaw, 1920).

46. M. Synofzik, W. M. C. van Roon-Mom, G. Marckmann, H. A. van Duyvenvoorde, H. Graessner, R. Schule, A. Aartsma-Rus, Preparing n-of-1 antisense oligonucleotide treatments for rare neurological diseases in Europe: Genetic, regulatory, and ethical perspectives. *Nucleic Acid Ther.* **32**, 83–94 (2022).

47. K. K. Aras, N. R. Faye, B. Cathey, I. R. Efimov, Critical volume of human myocardium necessary to maintain ventricular fibrillation. *Circ. Arrhythm. Electrophysiol.* **11**, e006692 (2018).

48. A. M. Gacita, D. E. Fullenkamp, J. Ohiri, T. Pottinger, M. J. Puckelwartz, M. A. Nobrega, E. M. McNally, Genetic variation in enhancers modifies cardiomyopathy gene expression and progression. *Circulation* **143**, 1302–1316 (2021).

49. D. E. Fullenkamp, A. B. Willis, J. L. Curtin, A. P. Amaral, K. T. Dittloff, S. I. Harris, I. A. Chychula, C. W. Holgren, P. W. Burridge, B. Russell, A. R. Demonbreun, E. M. M. Nally, Physiological stress improves stem cell modeling of dystrophic cardiomyopathy. *Dis. Model. Mech.* **17**, dmm050487 (2024).

50. P. W. Burridge, E. Matsa, P. Shukla, Z. C. Lin, J. M. Churko, A. D. Ebert, F. Lan, S. Diecke, B. Huber, N. M. Mordwinkin, J. R. Plews, O. J. Abilez, B. Cui, J. D. Gold, J. C. Wu, Chemically defined generation of human cardiomyocytes. *Nat. Methods* **11**, 855–860 (2014).

51. D. F. Selgrade, D. E. Fullenkamp, I. A. Chychula, B. Li, L. Dellefave-Castillo, A. D. Dubash, J. Ohiri, T. O. Monroe, M. Blancard, G. Tomar, C. Holgren, P. W. Burridge, A. L. George Jr., A. R. Demonbreun, M. J. Puckelwartz, S. A. George, I. R. Efimov, K. J. Green, E. M. M. Nally, Susceptibility to innate immune activation in genetically-mediated myocarditis. *J. Clin. Invest.* **134**, e180254 (2024).

52. J. T. Kim, W. Ouyang, H. Hwang, H. Jeong, S. Kang, S. Bose, S. S. Kwak, X. Ni, H. Kim, J. Park, H. Chen, A. Soetikno, J. Kim, S. Xu, L. P. Chamorro, J. A. Rogers, Dynamics of plosive consonants via imaging, computations, and soft electronics. *Proc. Natl. Acad. Sci. U.S.A.* **119**, e2214164119 (2022).

53. R. M. Geiger, M. G. Klein, N. Fatima, R. E. Goldstein, M. J. Krantz, M. C. Haigney, T. P. Flagg, Rapid assessment of proarrhythmic potential using human iPSC-derived cardiomyocytes. *JACC Clin. Electrophysiol.* **6**, 1860–1862 (2020).

54. Q. Wu, P. Zhang, G. O'Leary, Y. Zhao, Y. Xu, N. Rafatian, S. Okhovatian, S. Landau, T. A. Valiante, J. Travas-Sejdic, M. Radisic, Flexible 3D printed microwires and 3D microelectrodes for heart-on-a-chip engineering. *Biofabrication* **15**, 035023 (2023).

55. B. Gu, X. Li, C. Yao, X. Qu, M. Mao, D. Li, J. He, Integration of microelectrodes and highly-aligned cardiac constructs for in situ electrophysiological recording. *Microchem. J.* **190**, 108587 (2023).

56. M. Rieger, C. Dellenbach, J. Vom Berg, J. Beil-Wagner, A. Maguy, S. Rohr, Enabling comprehensive optogenetic studies of mouse hearts by simultaneous opto-electrical panoramic mapping and stimulation. *Nat. Commun.* **12**, 5804 (2021).

57. S. S. Nunes, J. W. Miklas, J. Liu, R. Aschar-Sobbi, Y. Xiao, B. Zhang, J. Jiang, S. Massé, M. Gagliardi, A. Hsieh, N. Thavandiran, M. A. Laflamme, K. Nanthakumar, G. J. Gross, P. H. Backx, G. Keller, M. Radisic, Biowire: A platform for maturation of human pluripotent stem cell–derived cardiomyocytes. *Nat. Methods* **10**, 781–787 (2013).